J. Phys. Chem. A **2009,** *113,* 5385–5396

Evidence of Formation of Bicyclic Species in the Early Stages of Atmospheric Benzene Oxidation

David R. Glowacki,[†] Liming Wang,[†,‡] and Michael J. Pilling*,[†]

School of Chemistry, University of Leeds, Leeds LS2 9JT, United Kingdom, and School of Chemistry and Chemical Engineering, South China University of Technology, Guangzhou, China, 51640

Received: January 7, 2009; Revised Manuscript Received: March 5, 2009

The oxidation of aromatic compounds in the troposphere substantially contributes to the formation of O_3 and secondary aerosol on a regional scale. Nevertheless, the initial stages of aromatic oxidation remain poorly understood. In this work, we present a quantitative analysis of previous experimental measurements relevant to atmospheric benzene oxidation. Using results from G3X(MP2), G3X(MP2)-RAD, CASSCF, and CASPT2 electronic structure theory, we have performed master equation (ME) calculations examining the kinetics of the benzene-OH adduct in the presence of O_2. Our results show the system to be complicated, with four isomers that may be formed following O_2 addition giving rise to multiple decay time scales of the benzene-OH adduct. We have examined the available experimental data in line with our findings and performed a sensitivity analysis of the agreement between the experimental and calculated kinetics with respect to uncertainties in the calculated stationary point energies. Our mechanism gives a phenol yield of 0.55 to 0.65, with the remainder giving a cis bridged bicyclic peroxy radical. Under atmospheric conditions, the epoxide yield is small. Distinct from the TST approaches and free energy surfaces available in previous studies, analysis of our ME results shows that several of the reactions occurring in this system are not at the high-pressure limit in the atmosphere.

Introduction

Volatile aromatic compounds are significant contributors to pollution and ozone formation in the troposphere. Houweling et al. have estimated that they make up 10% of nonmethane global anthropogenic VOC emissions,[1] mostly from car exhaust and solvent usage, and other estimates are larger.[2] However, they likely account for a much larger fraction of the tropospheric O_3 production than their mass emissions alone would suggest because of their high O_3-forming potential. For an air mass typical of northwest Europe, Derwent et al. estimated that aromatic species may be responsible for up to 30% of O_3 formation.[3] Besides the fact that high concentrations of O_3 have been shown to have an adverse affect on human health and vegetation,[4] there are other aspects of tropospheric aromatic oxidation that may impact human health. For example, benzene is a known carcinogen,[5] and some of the proposed degradation products in aromatic oxidation have toxic and mutagenic properties.[6] Aromatic oxidation processes have also been identified to contribute to secondary organic aerosol (SOA) formation.[2,7] The impact of aerosol formation is a significant uncertainty in climate change models, and recent research has provided increasing evidence linking fine particulate matter to deleterious effects on human health and premature deaths.[8]

Despite the significance of tropospheric aromatic oxidation to air quality models and associated consequences for human health, the detailed mechanism of aromatic oxidation is poorly understood.[4,9] For example, the Master Chemical Mechanism (MCMv3.1),[4,9−11] which is an atmospheric chemistry model that provides the most explicit representation of the constituent reactions involved in aromatic oxidation, is unable to describe key experimental observations in smog chamber studies: it significantly overestimates ozone formation and underestimates OH production.[4] Because of the lack of fundamental mechanistic understanding, many mechanisms used for modeling aromatic atmospheric chemistry deploy parametrized aromatic VOC oxidation chemistry that has been fitted to experimental data sets.[12] Clearly, a more fundamental understanding of the elementary reactions involved in the gas-phase atmospheric oxidation of aromatic species is desirable. An understanding of the reaction mechanism should also help to identify intermediates significant to SOA formation.[13,14]

Several previous experimental and theoretical studies have been carried out to unravel the elementary reactions involved in aromatic oxidation. Many experimental studies have focused on the more reactive aromatic hydrocarbons such as toluene and xylene.[7,13,15−19] These studies are complicated because of difficulties in the direct observation of the highly reactive intermediates formed during the oxidation. Electronic structure theory investigations of these systems are similarly difficult because of the size of the system, the large number of isomeric reaction paths available, and non-negligible multireference character of the molecular wave functions.

Given the aforementioned difficulties, the study presented herein addresses the simplest aromatic system: benzene. The tropospheric oxidation of benzene is initiated exclusively through reaction with OH[5,20] to give a benzene-OH adduct, $C_6H_6{-}OH$, under atmospheric conditions[21−24]

$$OH + C_6H_6 \rightleftarrows C_6H_6{-}OH \qquad (R1)$$

O_2 may then reversibly add to the $C_6H_6{-}OH$ adduct to give a peroxy radical, $\cdot RO_2$. Recent experimental work by Koch et al.[15] has shown that the benzene-OH adduct exclusively reacts

---

* Corresponding author. E-mail: M.J.Pilling@leeds.ac.uk.
[†] University of Leeds.
[‡] South China University of Technology.

10.1021/jp9001466 CCC: $40.75

with O_2 and that reaction with NO_2 is negligible under atmospheric conditions

$$C_6H_6{-}OH + O_2 \rightleftarrows RO_2 \qquad (R2)$$

Previously obtained experimental kinetics traces[22,25−27] for $C_6H_6{-}OH$ show an equilibrium, which has been attributed to reaction R2; however, these studies have confirmed that the observed kinetics traces for $C_6H_6{-}OH$ cannot be solely explained by reaction R2. Analysis of the decay traces suggests an irreversible loss from the equilibrium: either an irreversible reaction of $C_6H_6{-}OH$ with O_2 or an irreversible unimolecular reaction of RO_2

$$C_6H_6{-}OH + O_2 \rightarrow \text{products} \qquad (R3)$$

$$\cdot RO_2 \rightarrow \text{products} \qquad (R4)$$

In addition to investigations of the kinetics of benzene oxidation, product measurements have identified both glyoxal and phenol as primary products in benzene oxidation.[5,20,28−30] The proposed products of reactions R3 and R4 are phenol + HO_2 and a bicyclic species featuring an O−O peroxide bridge, respectively. The latter offers a potential route to glyoxal formation.[2] Previous semiempirical and B3LYP/6-311+G(d,p)//B3LYP/6-31+G(d) studies of reactions R1−R4 have been undertaken by both Lay et al.[31] and Tonachini and coworkers.[6,32,33] While these studies are useful for providing a qualitative mapping of the benzene oxidation potential energy surface, B3LYP and semiempirical PM3 energies are generally not sufficiently accurate for investigating quantitative agreement between experimental data and kinetics modeling.[34] Indeed, the inaccuracies of the energies calculated in the above studies have been noted by Bohn and Zetzsch,[22] who point out that the enthalpy change of reaction R2 calculated by Lay et al.[31] and Ghigo and Tonachini[32] disagree by 40 kJ mol^{-1}, with the semiempirical energy of Lay et al. giving better agreement with their experiments. Tonachini and coworkers[6,32,33] proposed that $\cdot RO_2$ reacts with NO to give NO_2, followed by ring-opening; however, considering that the pseudo-first-order loss rate of $C_6H_6{-}OH$ and the $\cdot RO_2$ species in air has been shown to be ~1000−2000 s^{-1}, this mechanism would require atmospheric [NO] of greater than 1 ppm, and is therefore unlikely under atmospheric conditions.[22,25] Therefore, the theoretical studies mentioned above have not produced a reaction mechanism for the OH-initiated oxidation of benzene that quantitatively accounts for the experimentally observed kinetics and product yields.[20,25,29]

Raoult et al. investigated the initial stages of the benzene oxidation process in a combined experimental and theoretical study.[25] These workers measured the kinetic decay of $C_6H_6{-}OH$ and obtained results in agreement with those obtained by Bohn and Zetzsch.[22] They carried out transition-state theory (TST) calculations for reactions R2, R3, and a few select R4 channels utilizing a CCSD(T)/6-31G(d,p)//B3LYP/6-31G(d) model chemistry for stable species and their own intrinsic method (IM) for transition states.

Starting with reaction R1, the mechanism proposed by Raoult et al. is as follows

$$\cdot C_6H_6{-}OH + O_2 \rightarrow \text{phenol} + HO_2 \qquad (R5)$$

$$\cdot C_6H_6{-}OH + O_2 \rightleftarrows \cdot RO_2(\text{ortho-trans}) \qquad (R6)$$

$$\cdot C_6H_6{-}OH + O2 \rightleftarrows \cdot RO_2(\text{ortho-cis}) \qquad (R7)$$

$$\cdot RO_2 \rightarrow \text{products} \qquad (R8)$$

where ortho-trans and ortho-cis indicate the position of O_2 with respect to OH. The TST rate coefficients calculated by these authors give kinetic traces of $C_6H_6{-}OH$ in good agreement with those measured experimentally; however, their forward rate coefficient for reaction R6 is ~2 orders of magnitude larger than that of reaction R7, such that reactions R5 and R6 dominate reaction R7. Because the rate coefficient for RO_2(ortho-trans) isomerization to give a bicyclic oxidation product is substantially smaller than the rate at which RO_2(ortho-cis) undergoes the same isomerization process, Raoult et al. note that their mechanism does not give an appreciable yield of the bicyclic oxidation product.

A mechanism that does not readily account for a high yield of a bicyclic species makes it difficult to rationalize the formation of experimentally observed dicarbonyl products such as glyoxal. In this work, we have revisited the mechanism for the initial stages of benzene oxidation using single and multireference electronic structure theory calculations performed at a higher level than those previously reported. We have calculated several stationary points on the PES for reactions R5−R8 using three different model chemistries: G3X(MP2),[35] G3X(MP2)-RAD,[36] and multireference second-order perturbation theory[37,38] using a complete active space (CAS) wave function. Using the energy-grained master equation (ME) in an approach similar to that described in recent work,[39−42] we have calculated rate coefficients, time-dependent species profiles, and product branching ratios. Additionally, we have performed a sensitivity analysis of our stationary point energies with respect to the available experimental data.

Utilizing our PES calculations, we find the system to be substantially more complex than previous workers have supposed, with different isomers formed on different time scales, giving rise to complex multiexponential time traces. We have reinterpreted the available experimental data in accord with our findings and show that within the error limits of the model chemistries utilized, agreement between our model and the reinterpreted experimental data is good, providing evidence for a mechanism going via a cis bicyclic ring. In addition, our ME model suggests that not all of the reactions in this system are at the high-pressure limit at atmospheric pressure. This is a particularly interesting feature of this system because the free energy surfaces calculated in the work of Tonachini and coworkers, and the TST rate constants calculated by Raoult et al. both assume that Maxwell−Boltzmann statistics dominate the reaction dynamics; that is, the system is at its high-pressure limit at atmospheric pressure.

Methods

I. Electronic Structure Calculations. The shortcomings of DFT energies for obtaining the sort of PES accuracy required for investigating quantitative agreement between kinetics calculations and experimental data were discussed above. Another complication relevant to a theoretical investigation of this system is the substantial multireference character of the wave function. Many of the structures in this work have nonequivalent resonance structures and significant delocalization of the valence electrons. As discussed by Tonachini and coworkers[6,32,33] and Raoult et al.,[25] these effects are particularly important for transition-state (TS) structures on the benzene-OH + O_2 PES, with several of these structures having significant spin contamination in unrestricted calculations. For restricted closed-shell Hartree−Fock (RHF) or restricted open-shell HF (ROHF) wave functions, the use of a single determinant wave function to calculate TS energies often fails to account for electron delocalization, leading to an overprediction of barrier heights.[25,36,43,44]

Complete basis set (CBS) CCSD(T) extrapolations on a system of this size are not presently feasible, and similar to recent theoretical work carried out by Klippenstein and coworkers on cyclohexyl + O_2, we utilize a member of the G*n* family of methods. The goal of the G3X method is to approximate a QCISD(T)/G3XL model chemistry, where G3XL refers to the G3XLarge basis set, which is a 6-311+G(3d2fg,2df) Pople basis.[35] In the G3X(MP2) method, geometry optimizations are carried out at the B3LYP/6-31G(2df,p) model chemistry, and a series of single-point post-SCF energy calculations are carried out on the DFT geometry. For molecules that feature atoms no larger than those in the second row, the G3X(MP2) zero-point energy is determined as follows

$$E_0[\mathrm{G3X(MP2)}] = \mathrm{MP4/6\text{-}31G(d)} + \Delta E(\mathrm{CC}) + \Delta E(\mathrm{MP2}) + \Delta E(\mathrm{G3XLarge}) + E(\mathrm{HLC}) + E(\mathrm{ZPE}) \quad \mathrm{(E1)}$$

where ΔE(CC) is a correction for correlation effects beyond fourth-order perturbation theory, ΔE(MP2) is a correction for the differences introduced by the much larger G3MP2L basis set with respect to the 6-31G(d) basis, and ΔE(G3XLarge) is a correction for larger basis set effects beyond G3MP2L. *E*(HLC) is the higher level correction, which has been optimized to give the best possible agreement between the calculations and the data included in the G3/99 test set.[46] The zero-point energy correction, *E*(ZPE), is determined by scaling the calculated B3LYP/6-311+G(3df,2p) frequencies by 0.9854. All G3X(MP2) calculations were carried out using the Gaussian 03 program suite,[45] and all stationary points were visualized with GaussView.[47] All of the TS geometries reported in this work are saddle points with one negative frequency. In those cases where inspection of the normal mode displacement vector corresponding to the reaction coordinate was ambiguous, an intrinsic reaction coordinate (IRC) calculation was carried out to map the minima on either side of the TS.

For open-shell species, the G3X(MP2) protocol indicates that the post HF calculations in eq E1 feature an unrestricted HF (UHF) calculation. Whereas UHF wave functions allow electron delocalization with respect to the ROHF wave function, they do not rigorously conserve spin symmetry and may be contaminated by higher spin states that can affect the calculated energies.[48] The G3X(MP2)-RAD model chemistry is a variant of G3X(MP2) theory designed for open-shell species in those cases where spin contamination in the UHF G3X(MP2) wave function suggests that the calculated energies may not be reliable.[36] For all post-SCF calculations, the G3X(MP2)-RAD method replaces the UHF wave function with a restricted open-shell HF (ROHF) calculation. The QCISD(T) calculation is replaced by a UCCSD-ROHF calculation, available in Molpro.[49] All UMP2/ROHF calculations were carried out using G03.

For the multireference results that we report, all CASSCF calculations were carried out using the cc-pVDZ basis set of Dunning,[50] which was the largest that our computational facilities would permit. CASSCF geometry optimizations were followed by frequency calculations, and the displacement vector corresponding to the negative eigenvalue was inspected to verify that TSs did indeed connect the minima indicated. For all of the CASSCF calculations, the natural orbitals obtained from diagonalization of the electron density matrix were visualized using MOLDEN[51] to ensure that the active space remained consistent for all geometries. For each orbital included in the active space, the natural orbital occupation numbers obtained from the diagonalization of the electron density matrix ranged between 0.02 and 1.98.[48] Dynamical electron correlation was recovered using multireference Rayleigh−Schrodinger second-order perturbation theory (henceforth, CASPT2).[37,38] In the CASPT2 calculations, all electron excitations were considered within the CASSCF active space. The electrons residing in all other occupied orbitals (not including the core orbitals) were correlated through single and double excitations. All multireference calculations were performed using the MOLPRO program suite.[49] Finally, apart from O_2, which was calculated with $^3\Sigma_g^-$ symmetry, the reported results feature wave functions with no spatial symmetry.

II. Master Equation Calculations. The form of the energy-grained ME used in this work has been described in detail previously.[52−54] The phase space for each isomer was divided into energy grains with a width of 50 cm^{-1}. Collisional energy transfer in the grained phase space and interconversion between species was described with a set of coupled differential equations. Briefly, the form used in this work is

$$\frac{\mathrm{d}}{\mathrm{d}t}\mathbf{p} = \mathbf{M}\mathbf{p} \qquad \mathrm{(E2)}$$

where **p** is the population vector containing the populations of the energy grains for the *i*th isomer, $n_i(E)$, and **M** is the matrix that determines population evolution due to collisional energy transfer and reaction. Collisional energy transfer was described using an exponential down model, parametrized with Lennard-Jones parameters (given in the Supporting Information), and the average downward energy transferred ($<\Delta E>_{\mathrm{down}} = 250$ cm^{-1}, typical of a N_2 bath gas). Microcanonical RRKM rate constants were calculated using vibrational harmonic oscillator approximations and by treating all molecules as either 2D or 3D classical free rotors. The relevant molecular parameters are given in the Supporting Information to this article.

The discretized matrix **M** was diagonalized, and the eigenpairs were determined to give a solution of the form

$$\mathbf{p} = \mathbf{U}e^{\lambda t}\mathbf{U}^{-1}\mathbf{p}(0) \qquad \mathrm{(E3)}$$

where **p**(0) contains the initial conditions (i.e., $t = 0$) for each grain (i.e., $n_{iE}(0)$), **U** is the matrix of eigenvectors obtained from diagonalization of **M**, and λ represents the corresponding eigenvalues. Within our formulation of the ME, products are represented using the infinite sink approximation. The normalized time-dependent product concentration, $P(t)$, is

$$P(t) = 1 - \sum_i \sum_E n_{iE}(t)\,\mathrm{d}t \qquad \mathrm{(E4)}$$

If only one product channel is available, then eq E4 provides information regarding the time-dependent product yield; however, when there are p products, the normalized yield of a specific product at time t, $P_{pi}(t)$, may be written as

$$P_{pi}(t) = \left[\frac{\sum_{t} [\sum_{E} k_{pi}(E) n_{iE}(t)\, \mathrm{d}E]\, \mathrm{d}t}{\sum_{p} [\sum_{t} [\sum_{E} k_{pi}(E) n_{iE}(t)\, \mathrm{d}E]\, \mathrm{d}t]} \right] P(t) \quad \text{(E5)}$$

where $n_{iE}(t)$ is the time-dependent population of the energy grains spanning the entire state space of the ith well obtained from eq E3, and $k_{pi}(E)$ represents the microcanonical rate constants for the formation of product p from isomer i.

To analyze the available experimental kinetics data, the microcanonical information contained in the ME solution eq E3 must be transformed to phenomenological rate coefficients, and the procedure we use for doing so utilizes an eigenvector/eigenvalue analysis similar to that described by Bartis and Widom.[53,55,56] All ME calculations and the eigenvalue−eigenvector analysis were carried out using our recently developed MESMER program.[57]

Results and Discussion

I. Electronic Structure Calculations. There are four possible paths for the addition of O_2 to the benzene-OH adduct: cis or trans, and ortho or para. The G3X(MP2)-RAD stationary points involved in the cis para (**c-p**), trans para (**t-p**), ortho cis (**c**), and ortho trans (**t**) addition pathways are shown in Figure 1. Table 1 gives the corresponding G3X(MP2) and G3X(MP2)-RAD energies, spin expectation values ($<S^2>$), and T1/D1 diagnostics[58] obtained from the UQCISD(T) and CCSD(T) calculations. In Figure 1 and Table 1, all energies are referenced to **I2-c-ax**. In all of the Figures, **I** denotes an intermediate and **TS** denotes a transition state. **I1** is the benzene-OH adduct, and **I2** represents isomers formed following the addition of O_2 to **I1**.

Inspection of Figure 1 shows two different cis ortho isomers: **I2-c-ax**, wherein the O_2 is in the axial position (denoted by **ax**), and **I2-c-eq**, in which the O_2 is equatorial (**eq**). **I2-c-ax** and **I2-c-eq** may isomerize via **TS-c(eq-ax)**, as shown in Figure 1. Similarly, trans (**t**) addition of O_2 gives two different isomers: **I2-t-ax** may isomerize via **TS-t(eq-ax)** to give **I2-t-eq**. Also shown in Figure 1 are the TSs for the formation of phenol + HO_2: **TS1-HO$_2$** is a direct abstraction of the hydrogen ipso to OH, and **TS3-HO$_2$** is a concerted elimination of HO_2 that is only possible from **I2-t-ax**. The ortho addition channels give more stable structures than para channels because of hydrogen bonding between the O−O and the O−H. Apart from redissociation, there are no energetically accessible reaction paths available to the para adducts; nevertheless, as will be shown below, they may be important to the kinetics.

Isomerization pathways leading to bridged ring structures are possible when O_2 is in the axial position, and the possible rings that may be formed are shown in Figure 1. If the OH position is at carbon 1, bicyclic rings may be formed with O−O links between carbons 2 and 6 (**2,6**), 2 and 3 (**2,3**), and 2 and 4 (**2,4**). For both the cis and the trans pathways, the (**2,6**) pathway is the most kinetically facile. Transition states and intermediates corresponding to a hydrogen transfer that convert the peroxy radical to an oxy hydroperoxide radical are also shown in the Figure 1 and are denoted by **OOH**. As inspection of the structures shown in the Figure 1 indicates, this transition state is not available for **I2-t-ax**, wherein both the O_2 and the OH are situated axially. **TS4-c** is the transition state in which the O−O bond in **I3-c-2,6** breaks, leading to an epoxide. This channel is further discussed below. We were unable to locate an analogous TS from **I3-t-2,6** for **TS4-t**, but given that dissociation via **TS3-HO$_2$** dominates isomerization via **TS3-t-ax-2,6**, subsequent reactions of **I3-t-2,6** do not appear to be significant.

Besides identifying several more isomers, the PES stationary points shown in Figure 1 have two important differences with respect to those calculated by Raoult et al. First, the entrance barrier for cis addition of O_2 is lower in energy than that for trans addition. There are two different TS structures for the cis addition. **TS1-c(i)** is lower in energy and has a geometry similar to TS(B) located by Ghigo and Tonachini.[32] Figure 2 shows the relative energies of **TS1-c(i)** and **TS1-c(ii)** in a relaxed scan about the torsional coordinate at the TS bond distance. On the PES of Raoult et al., the barrier to cis addition is larger than that for trans addition, almost certainly because the TS geometry they located corresponds to **TS1-c(ii)**. Second, Raoult et al. reported that their calculated barrier for the concerted elimination leading to HO_2 + phenol was too high for it to be significant (>83 kJ mol^{-1}). Our calculations show this channel (**TS3-HO$_2$**) to have a substantially smaller barrier, and, as will be discussed below, the calculations performed herein suggest that it may compete with the direct abstraction via **TS1-HO$_2$**.

The T1 and D1 diagnostics are designed to indicate the reliability of a CCSD calculation. For closed-shell species, if T1 < 0.02, then the CCSD(T) method is expected to give results close to the full CI limit for closed-shell species.[48] D1 is a similar diagnostic to T1, but it has been specifically designed for open-shell species; however, it generally shows a very strong correlation with T1.[58] Many of the T1 diagnostics for the structures on the PES in Figure 1 are larger than 0.02. This fact, alongside the large values of $<S^2>$ for the UHF calculations, suggests that multireference effects for many of the structures on this PES may be important.[44] For those stationary point geometries where $<S^2>$ is within 5% of the theoretical value, the G3X(MP2) and G3X(MP2)-RAD energies generally agree to within ∼2 kJ/mol. Lee suggested that the ratio, T1/D1, provides information regarding the homogeneity of a molecular system's electronic structure.[58] A ratio substantially smaller than $1/\sqrt{2}$ indicates that the coupled cluster calculation is having problems with a particular part of the molecule's electronic structure. For nearly all of the structures on this surface, the T1/D1 ratio is ∼0.16 to 0.20, suggesting significant heterogeneity of the electronic structure, likely due to nontrivial multireference character introduced by delocalization effects in the conjugated π system.

The multireference effects discussed above impact the exothermicity of the O_2 + **I1** reaction to give **I2-c-ax** and **I2-t-ax**, which is essential for understanding the experimentally investigated equilibrium of reaction R2. The **I1** equilibrium observed by Lesclaux and coworkers was attributed to **I1** + $O_2 \leftrightarrows$ **I2-t-eq**.[25,26] Using experimentally determined equilibrium constants and a calculated value of $\Delta S^0_{298} = -161.5$ J mol^{-1} K^{-1} (in nearly identical agreement with the corresponding values obtained in this work), they determined ΔH^0_{298} to be −52.3 kJ mol^{-1}, which is in good agreement with the G3X(MP2) energies given in Table 2. Most notable in this table is the fact that the G3X(MP2)-RAD energies differ by ∼10 kJ mol^{-1} from the corresponding G3X(MP2) energies. The discrepancy appears to arise from the difference between the ΔE(MP2) corrective term for the adducts and for **I1** + O_2. This likely arises from the fact that an accurate description of the binding energy using a single determinant wave function requires excitations larger than the doubles available in ROMP2. Using the DFT calculated ZPEs, a UCCSD(T)-ROHF/aug-cc-pVDZ calculation of ΔE_0(0K) for **I1** + $O_2 \leftrightarrows$ **I2-c-ax** gives a value of −41 kJ mol^{-1},

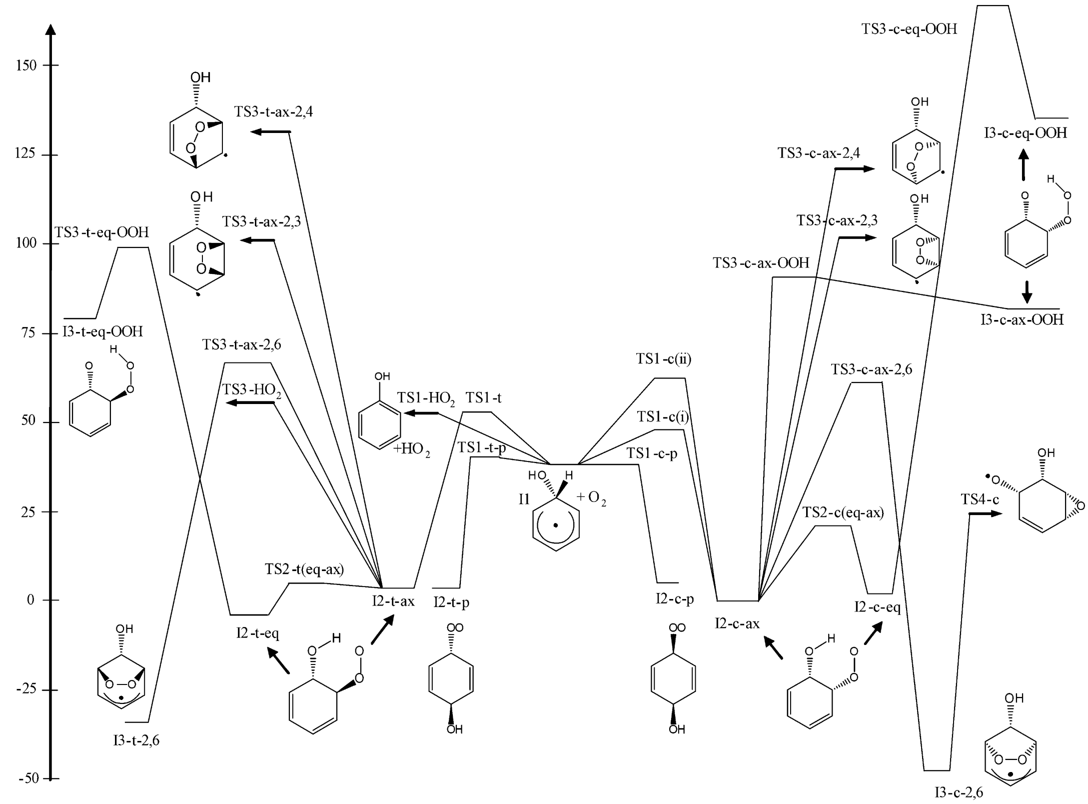

Figure 1. G3X(MP2)-RAD PES and structures for cis and trans addition pathways of O_2 to **I1**. Also shown is the direct abstraction channel to give phenol + HO_2. All energies are in kJ mol^{-1} and are referenced to **I2-c-ax**.

which lies between the G3X(MP2) and G3X(MP2)-RAD values. The unrestricted G3X(MP2) energies are likely able to describe some of the multireference character in the wave function of **I1** and **I2-c-ax**, but spin contamination in the UHF description of **I1** results in a slight overprediction.

Spin contamination deriving from state mixing that correlates with the addition of O_2 $^1\Delta_g$ to **I1** is responsible for the very high G3X(MP2) barrier height energies of **TS1-c(i)**, **TS1-c(ii)**, **TS1-t**, and **TS1-HO$_2$**.[59] For these structures, the wave function for the G3X(MP2)-RAD UCCSD(T)-RHF calculations is far more reliable, and the UCCSD(T) calculations are only slightly spin contaminated. The same is true for the calculated barrier heights of **TS3-t-ax-2,6**, **TS3-c-ax-2,6**, and **TS3-HO$_2$**, which are significant to understanding branching between phenol and bicyclic products.

To investigate multireference effects on the calculated energies, we examined three different sets of PES stationary points using a CASSCF wave function: (1) **I2-t-ax** → **TS3-t-ax-2,6** → **I3-t-2,6**; (2) **I2-c-ax** → **TS3-c-ax-2,6** → **I3-c-2,6**; and (3) **I2-c-ax** → **TS3-c-ax-OOH**. For the first two portions of the PES, both **I2-c-ax** and **I2-t-ax** featured a CASSCF wave function that utilized a nine electron, nine orbital (9,9) active space. Using the numbering scheme given in the Supporting Information, the active space included the π and π^* orbitals deriving from the p orbitals of carbons 3−6, the σ and σ^* orbitals for the C2−O15 and O15−O16 bonds, and the singularly occupied molecular orbital (SOMO), which localizes the radical on O16 of the peroxy moiety. In **TS3-t-ax-2,6** and **TS3-c-ax-2,6**, formation of the bridged bicyclic species occurs as the peroxy radical SOMO overlaps with the π system. As **I2-t-ax** and **I2-c-ax** isomerize to form the respective bridged bicyclic structures, **I3-t-2,6** and **I3-c-2,6**, the SOMO is delocalized over C3 and C5 as σ and σ^* orbitals are formed between O16 and C6. The description of **I2-c-ax** → **TS3-c-ax-OOH** utilized an (11,11) CASSCF wave function. The active space for **I2-c-ax** utilized the π and π^* orbitals of carbons 3−6, the peroxy radical SOMO, and the σ and σ^* orbitals for O15−O16, C1−C2, and O12−H13. In **TS3-c-ax-OOH**, a nascent σ and σ^* orbital arises as the bond between O16 and H13 forms, and the radical center migrates to O12.

Most of the CI coefficients for the CASSCF single reference determinants have magnitudes of ~0.9, with several other electron configurations having CI coefficients whose absolute value is greater than 0.1. A table of CI coefficients and the corresponding electron configurations for **I2-c-ax**, **TS3-c-ax-2,6**, and **I3-c-2,6** is given in the Supporting Information, and the calculated multireference energies are shown in Table 3. Further multireference calculations were attempted to describe **I2-c-ax** → **TS1-c(i)** → **I1** + O_2 and **I2-t-ax** → **TS1-t** → **I1** + O_2; however, an accurate description of the energetics of this portion of the PES requires inclusion of the lone pairs on O15 and O16, which occupy the doubly occupied degenerate $\pi_u 2p_x$ and $\pi_u 2p_y$ orbitals in the separated O_2 molecule (which transform as B_{3u} and B_{2u}, respectively, in the D_{2h} Abelian point group symmetry utilized for O_2 in MOLPRO). Inclusion of lone pairs at large separations of O_2 and **I1** is not problematic but results in failed convergence of the CASSCF wave function within the addition complex. In those cases where the wave function did converge, inspection of the natural orbitals within the addition complex indicated that the active space was not consistent, and the calculated energies were not accurate.

The aforementioned difficulty is a general complication that arises in using multireference methods to describe the addition of O_2 to radicals to form a peroxy radical, that is, $O_2 + R\bullet \rightarrow RO_2$. The degeneracy of the $\pi_u 2p_x$ and $\pi_u 2p_y$ orbitals in the separated O_2 molecule is lifted in the RO_2 molecule, and the lone pairs localize on each oxygen atom. Because the orbitals containing the O_2 lone pairs are strongly occupied in the addition

TABLE 1: G3X(MP2)-RAD and G3X(MP2) Calculated Energies (kJ mol^{-1}, 0 K), Spin Expectation Values, and T1/Q1 Diagnostics for the Portion of the PES Where O_2 Adds ortho-cis, ortho-trans, and para to OH

	stationary point	G3X(MP2) energy	$<S^2>$[b]	T1[c]	G3X(MP2)-RAD energy	T1[d]	D1[d]	$<S^2>$[d]
	O_2 + I1[a]	48.16	0.872	0.032	37.76	0.016	0.608	0.766
	TS1-HO_2	92.304	1.993	0.036	54.65	0.034	0.219	0.933
cis ortho	TS1-c(i)	82.74	1.877	0.042	48.45	0.039	0.233	0.802
	TS1-c(ii)	98.00	1.961	0.039	65.20	0.044	0.282	0.876
	I2-c-ax	0.00	0.752	0.023	0.00	0.025	0.156	0.751
	TS2-c(eq-ax)	19.87	0.750	0.022	19.69	0.025	0.154	0.751
	I2-c-eq	7.12	0.752	0.023	6.91	0.025	0.157	0.751
	TS3-c-ax-2,6	72.34	1.011	0.043	63.57	0.036	0.225	0.775
	TS3-c-ax-2,3	120.38	0.980	0.047	104.12	0.042	0.274	0.785
	TS3-c-ax-2,4	150.14	1.007	0.057	129.00	0.037	0.213	0.774
	TS3-c-ax-OOH	93.76	0.778	0.038	91.48	0.040	0.265	0.755
	I3-c-ax-OOH	84.78	0.769	0.028	84.45	0.031	0.199	0.753
	TS3-c-eq-OOH	110.23	0.916	0.059	176.93	0.079	0.549	0.755
	I3-c-eq-OOH	97.13	0.912	0.050	139.71	0.044	0.297	0.753
	I3-c-2,6	−43.028	0.759	0.024	−48.87	0.014	0.048	0.752
	TS4-c	63.56	1.392	0.044	25.01	0.042	0.249	0.805
trans ortho	TS1-t	89.35	1.891	0.041	54.54	0.039	0.231	0.819
	I2-t-ax	4.50	0.752	0.023	4.44	0.025	0.147	0.751
	TS2-t(eq-ax)	5.31	0.750	0.023	5.23	0.025	0.148	0.751
	I2-t-eq	−4.89	0.752	0.023	−5.04	0.025	0.153	0.751
	TS3-HO_2	96.388	1.800	0.042	58.50	0.049	0.325	0.775
	TS3-t-ax-2,6	78.43	0.951	0.046	68.98	0.030	0.175	0.763
	TS3-t-ax-2,3	118.73	0.980	0.046	104.75	0.040	0.255	0.782
	TS3-t-ax-2,4	156.86	0.983	0.061	134.45	0.036	0.205	0.774
	TS3-t-eq-OOH	99.67	0.751	0.046	101.80	0.080	0.545	0.760
	I3-t-eq-OOH	87.08	0.936	0.051	81.44	0.038	0.250	0.755
	I3-t-2,6	−28.604	0.759	0.024	−34.56	0.015	0.055	0.757
para	TS1-t-p	71.38	1.842	0.040	40.78	0.038	0.228	0.836
	TS1-c-p	67.24	1.851	0.040	37.04	0.039	0.242	0.837
	I2-t-p	−1.03	0.752	0.025	4.09	0.024	0.139	0.751
	I2-c-p	−2.87	0.752	0.028	7.25	0.024	0.140	0.751

[a] Q1, T1, and $<S^2>$ expectation values are for I1. For O_2, these values were not problematic. [b] Expectation value of the spin operator of the UHF/6-31G(d) reference wave function (used in the UQCISD(T) calculation) after annihilation of the major spin contaminant and correction to first order. [c] Obtained from UQCISD(T) calculation. [d] Obtained from RCCSD(T) calculation.

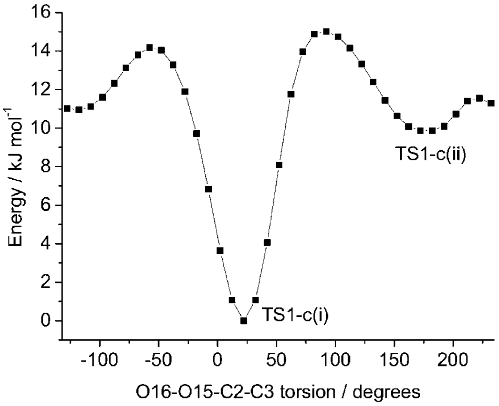

Figure 2. Results of a relaxed UB3LYP/6-31G(2df,p) torsional scan about the O16−O15−C2−C3 dihedral angle for ortho-cis addition of O_2 to **I1**. See the Supporting Information for the atom labeling scheme. Both **TS1-c(i)** and **TS1-c(ii)** are shown.

complex, their inclusion within the active space causes CASSCF convergence problems. An alternative strategy to including the lone pair orbitals within the CASSCF active space is to include them within the reference space for a post CASSCF calculation, such as CASPT2 or multireference configuration interaction (MRCI).[59] When the peroxy radical is small, it is straightforward to identify the orbitals in which the lone pairs reside, and our own unpublished results using this methodology show that multireference calculations performed on acetylene-OH + O_2 → RO_2 and acetyl + O_2 → RO_2 give sensible energies. However, in the case of **I1** + O_2 → RO_2, there is significant mixing between orbitals, and those in which the lone pairs reside are not easy to identify, even with an expanded active space. Because the lone pairs on O15 and O16 remain essentially localized in all molecular geometries, the multireference results given in Table 3 are not subject to the complications discussed above. Therefore, the multireference energies in Table 3 agree reasonably well with the G3X(MP2)-RAD results in Table 1.

TABLE 2: Calculated Values of ΔE (0 K) and ΔH^0 (298 K) for I2-c-ax, I2-c-eq, I2-t-ax, and I2-t-eq, Referenced to I1 + O_2 in Units of kJ mol^{-1}

	stationary point	I2-c-ax	I2-c-eq	I2-t-ax	I2-t-eq
G3X(MP2)	ΔE (0 K)	−48.16	−41.04	−43.66	−53.05
	ΔH^0 (298 K)	−51.73	−44.16	−46.42	−56.61
G3X(MP2)-RAD	ΔE (0 K)	−37.76	−30.85	−33.32	−42.80
	ΔH^0 (298 K)	−41.33	−33.97	−36.09	−46.36

Table 3 shows that the CASPT2 calculations give a 0 K barrier height for **I2-t-ax** → **TS3-t-ax-2,6** of 63.40 kJ mol^{-1}, which is in good agreement with the G3X(MP2)-RAD value of 64.54 kJ mol^{-1} and that calculated by Raoult et al. Similarly, the CASPT2 **I2-c-ax** → **TS3-c-ax-OOH** barrier height is 84.83 kJ mol^{-1}, which is in reasonable agreement with the G3X(MP2)-RAD value of 91.48 kJ mol^{-1}. For **I2-c-ax** → **TS3-c-ax-2,6**, the CASPT2 barrier height of 48.35 kJ mol^{-1} is smaller than both the G3X(MP2) RAD value of 63.57 kJ mol^{-1} and the value of 57.7 kJ mol^{-1} calculated by Tonachini and coworkers but larger than the value of 37.7 kJ mol^{-1} calculated by Raoult et

TABLE 3: Multireference Results for Three Different Portions of the 0 K PES Discussed Above[a]

PES path	stationary point	CASSCF E_0 + G3X E_{ZPE}/kJ mol^{-1}	CASPT2 E_0 + G3X E_{ZPE}/kJ mol^{-1}
1	I2-c-ax	0.00[b]	0.00[c]
	TS3-c-ax-2,6	65.20[b]	48.35[c]
	I3-c-2,6	−39.09[b]	−57.48[c]
2	I2-t-ax	5.94[b]	8.56[c]
	TS3-t-ax-2,6	84.90[b]	71.96[c]
	I3-t-2,6	−25.13[b]	−42.70[c]
3	I2-c-ax	0.00[d]	0.00[e]
	TS3-c-ax-OOH	128.90[d]	84.83[e]

[a] Energies shown have been corrected using the G3X zero-point energy (ZPE). [b] Referenced to CASSCF(9,9) **I2-c-ax** energy. [c] Referenced to CASPT2(9,9) **I2-c-ax** energy. [d] Referenced to CASSCF(11,11) **I2-c-ax** energy. [e] Referenced to CASPT2(11,11) **I2-c-ax** energy.

al. As discussed by Raoult et al., the fact that the barrier to forming the (2,6) ring is smaller for RO_2(cis) than RO_2(trans) is likely due to stabilization by hydrogen bonding type interactions that occur only in the cis geometry. The increased CASPT2 stabilization of **I3-c-2,6** and **I3-t-2,6** compared with their G3X(MP2)-RAD energies is likely due to effects resulting from delocalization of the lone electron over the π system, for which the multireference calculations provide a better description.

II. Master Equation Calculations. Despite the potential sources of error discussed above, a qualitative description of the significant features for describing the initial steps of benzene-OH + O_2 does emerge from these calculations: after OH adds to benzene, there are four possible O_2 addition paths. The barriers to para addition are very small, but there are no other energetically accessible reaction paths available to the para adducts other than redissociation to **I1** + O_2. For ortho addition, the cis transition state is lower in energy than that for the trans addition. For cis RO_2, isomerization to form the bridged bicyclic species is the route with the lowest TS energy. For the trans RO_2, dissociation to form phenol + HO_2 is the path with the lowest TS energy. Additionally, O_2 may abstract a hydrogen from **I1** to give HO_2 + phenol. Paths leading to 2−3 and 2−4 rings, as well as those involving H transfer to give OOH species, are insignificant with respect to the other reaction pathways in Figure 1.

The published experimental kinetic investigations of this system observe the decay kinetics of the benzene-OH adduct, **I1**, to obtain the equilibrium constant for $\cdot C_6H_6{-}OH + O_2 \leftrightarrows \cdot RO_2$. The mechanisms utilized by Grebenkin and Krasnoperov[27] as well as Bohn and Zetzsch[22] to explain their experimental data do not distinguish between the cis and trans isomers of $\cdot RO_2$. Only Raoult et al. suggested that the observed equilibrium exclusively involved the trans isomer, citing its greater stability and smaller barrier height for formation. Our calculations similarly indicate that the trans isomer, **I2-t-eq**, is more stable than **I2-c-ax**; however, as discussed above, we assign a smaller barrier to the formation of RO_2(cis). Furthermore, our calculations suggest two channels for phenol + HO_2 formation: (1) a concerted HO_2 elimination from RO_2(trans) via **TS3-HO$_2$**, and (2) a direct abstraction from **I1** via **TS1-HO$_2$**. The relative significance of both of these channels is discussed below.

In our previously published work,[52,60,61] the mean absolute deviations[20] of the composite G3X methods have been used as error limits for adjusting calculated energies to perform sensitivity analyses with respect to kinetics data, and we have performed a similar analysis in this article. To make the ME calculations less expensive, we made three simplifications to the PES shown in Figure 1: (1) Using the G3X(MP2)-RAD data, the forward and reverse TST unimolecular rate constants for **I2-c-ax** $\leftrightarrows$ **I2-c-eq** are greater than 10^8 s^{-1}, with >90% of the RO_2(ortho cis) existing as **I2-c-ax** at equilibrium. Similarly, the forward and reverse TST rate constants for **I2-t-ax** $\leftrightarrows$ **I2-t-eq** are greater than 10^{10} s^{-1}, with >95% of the RO_2(trans) in **I2-t-eq**. According to the ME analysis discussed below, the **I2-c-ax** $\leftrightarrows$ **I2-c-eq** and **I2-t-ax** $\leftrightarrows$ **I2-t-eq** equilibria are orders of magnitude faster than the unimolecular reaction rate coefficients for other reaction paths available to these species. Therefore, to a good approximation, the species profiles in the cis and trans RO_2 isomers should be dominated by **I2-c-ax** and **I2-t-eq**, with negligible contributions from **I2-t-ax** and **I2-c-eq**, respectively. Over the temperature range we are investigating, we have confirmed that this approximation gives results that are essentially identical to those obtained by explicitly representing **I2-c-ax**, **I2-c-eq**, **I2-t-ax**, and **I2-t-eq**. However, this approximation may not be valid in high-energy nonthermal regimes. (2) Under atmospheric conditions, ME simulations show that the formation of **I3-t-2,6** is trivial and does not compete with the formation of phenol + HO_2 via **TS3-HO$_2$**. Therefore, we did not examine this barrier height in the sensitivity analysis. (3) The $k(E)$ values for **I3-c-2,6** going to **I2-c-ax** are several orders of magnitude smaller than those for the reaction via **TS4-c**. Test ME calculations show that the **I1** decay kinetics are not sensitive to the kinetics via **TS4-c**. Therefore, it is an excellent approximation to assume that once the RO_2 isomers cross **TS3-t-ax-2,6,** they will not return; that is, the crossing of these transition states may be treated as a sink.

With these simplifications, simulation of the dynamics over the PES shown in Figure 1 may be represented by a 1D ME simulation with four isomer wells (**I2-c-ax**, **I2-t-eq**, **I2-c-p**, and **I2-t-p**), a source term, and four sinks leading to product formation (loss via **TS1-HO$_2$**, **TS3HO$_2$**, **TS3-t-ax-2,6**, and **TS3-c-ax-2,6**).

The last row of **M** in eq E2 is a bimolecular source term, which reflects the pseudo-first-order rate at which the four different **I2** isomers are microcanonically populated by **I1** + O_2, which are assumed to be thermalized. We determined the time-dependent species profile for **I1** by extracting from **M** the solution to the source term differential equation. For **I2-c-ax**, **I2-t-eq**, **I2-p-c**, and **I2-p-t**, we determined the time-dependent species populations by summing the time-dependent grain populations for all grains corresponding to each isomer. Time-dependent product concentration profiles for products formed via **TS1-HO$_2$**, **TS3-HO$_2$**, **TS3-c-ax-2,6**, and **TS3-t-ax-2,6** were determined according to eq E5.

For this system, which contains four wells, a source term, and three product channels, a total of 40 phenomenological rates coefficients emerge from the eigenvalue−eigenvector analysis: 20 describe forward and reverse interconversion between the wells and source, and 20 describe rate coefficients from the wells and source to the available product channels. Many of the rate coefficients are small, and as discussed in the Supporting Information, the kinetics of the system may be well approximated using 11 rate coefficients: forward and reverse rate coefficients via **TS1-t**, **TS1-c(i)**, **TS1-t-p**, and **TS1-c-p** as well as forward rate coefficients via **TS3HO$_2$**, **TS1HO$_2$**, and **TS3-c-ax-2,6**.

Using the average of the G3X(MP2) and G3X(MP2)-RAD energies for **I1** + O_2 (43 kJ mol^{-1}), Figure 3 shows the ME-calculated **I1** profile without adjustments to the stationary point energies described in the sensitivity analysis below. This plot

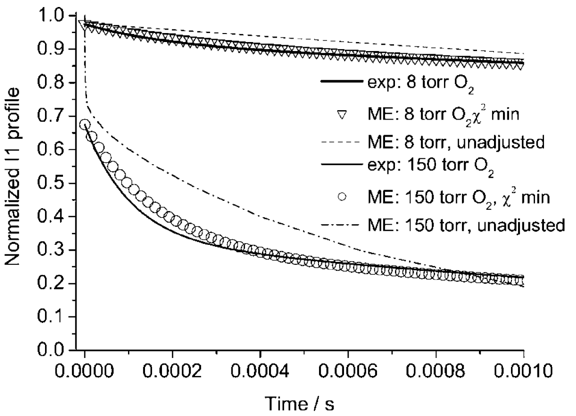

Figure 3. **I1** decay traces at 8 and 150 torr O_2. The dashed lines are from unadjusted ME calculations. The solid black and blue lines are the time-dependent profile of **I1** at the ME χ^2 minimum. ▽ and ○ correspond to the reinterpreted experimental data of Raoult et al. at both pressures.

shows the very fast initial decay of **I1** as the equilibrium with **I2-c-ax**, **I2-t-p**, and **I2-c-p** is established. The longer time decay occurs as equilibrium with **I2-t-eq** is established, and **I1** reacts irreversibly with O_2 to give phenol + HO_2 via **TS1-HO$_2$**. Therefore, there are multiple time scales for **I1** decay. Because Raoult et al. calculated a large barrier for **TS1-c** and did not consider para addition channels of O_2 to **I1**, they interpreted their experimental **I1** decay trace utilizing a biexponential kinetic model that includes only the two slowest decay time scales. This fact complicates a comparison of our multiexponential ME **I1** decay traces with the experimental biexponential decay traces. Therefore, we have reinterpreted the experimental data by assuming that the three fastest decay time scales of **I1** are faster than the experimental time scales. The mathematical details of our kinetic reinterpretation and a comparison of our analysis with previous analyses is given in the Supporting Information. It needs to be emphasized that experimental observation of the multiple time scale decay may be apparent as a different [**I1**] in the presence varying [O_2]; however, the difference would be subtle: no more than 10−20%, considering the sources of error in these calculations.

Given the previously discussed uncertainties in the calculated PES energies, we have conducted a sensitivity analysis, minimizing χ^2 to obtain the best fit of the ME-derived decay profile for **I1** to the reinterpreted experimental data. The stationary point energies examined in our sensitivity analysis are those with large $\langle S^2 \rangle$, T1, and D1 values and for which multireference results were not available for reasons discussed above. The energy of **I1** was varied between its G3X(MP2) and G3X(MP2)-RAD values. The energies of **TS1-HO$_2$**, **TS1-c(i)**, and **TS3-HO$_2$** were varied within their G3X(MP2)-RAD uncertainty limits (±5 kJ mol^{-1}). The fact that **TS1-c(i)** and **TS1-t** have $\langle S^2 \rangle$, T1, and D1 values that are nearly identical suggests that whereas their absolute energies are in error, there should be little relative error for these two geometries. Therefore, the energy of **TS1-t** was constrained to be 5 kJ mol^{-1} larger than the energy of **TS1-c(i)** on the basis of the result of the present calculations and in broad agreement with the calculations of Ghigo and Tonachini.[32] All energies were adjusted in steps of 1 kJ mol^{-1} such that the sensitivity analysis required more than 1500 ME calculations.

TABLE 4: Energy Ranges and χ^2 Minimum Values from the Sensitivity Analysis[a]

stationary point	lower bound	upper bound	χ^2 minimum value
I1 + O$_2$	37.76	48.16	44.00
TS1-c(i)	43.45	48.45	44.50
TS1-HO$_2$	51.65	56.65	55.65
TS3-HO$_2$	53.50	58.50	58.50

[a] All of the parameters are energies at 0 K in units of kJ mol^{-1} referenced to **I2-c-ax**.

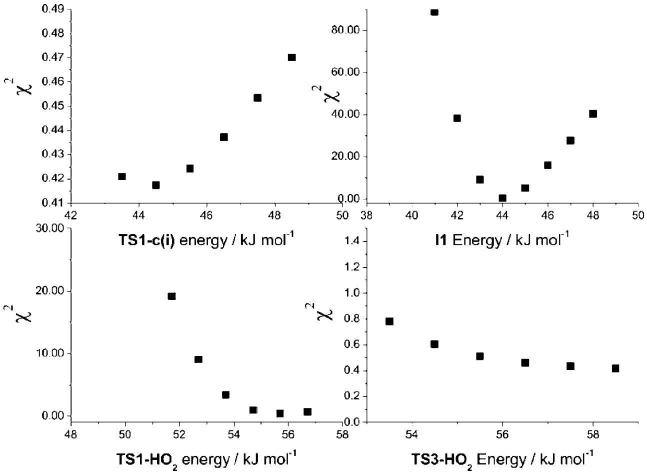

Figure 4. Sensitivity of χ^2 to stationary point energies at the global minimum.

TABLE 5: 298 K, 760 Torr Rate Coefficients Obtained from Bartis−Widom Eigenvalue−Eigenvector Analysis at the χ^2 Minimum[a]

reaction	rate coefficient
I1 + O_2 → **I2-c-ax**	2.80×10^{-15}
I2-c-ax → **I1** + O_2	9.76×10^{4}
I1 + O_2 → **I2-t-eq**	8.4×10^{-16}
I2-t-eq → **I1** + O_2	2.75×10^{3}
I1 + O_2 → **I2-t-p**	2.61×10^{-14}
I2-t-p → **I1** + O_2	4.79×10^{5}
I1 + O_2 → **I2-c-p**	4.15×10^{-14}
I2-c-p → **I1** + O_2	2.59×10^{6}
I1 + O_2 → phenol + HO_2	1.28×10^{-16}
I2-c-ax → **I3-c-ax-2,6**	3.07×10^{3}
I2-t-eq → phenol + HO_2	4.3×10^{1}

[a] Unimolecular rates are in units of s^{-1}, and bimolecular rate constants are in units of cm^3 molecule^{-1} s^{-1}.

Given their relatively small $\langle S^2 \rangle$, T1, and D1 values, the energies of **I3-c-ax**, **I3-t-eq**, **I2-t-p**, and **I2-c-p** were unadjusted and set as the average of their G3X(MP2) and G3X(MP2)-RAD energies. The rates through **TS1-t-p** and**TS1-c-p** are fast, even with their large multireference diagnostics. Because their energies do not have a significant effect on the **I1** decay on the experimental time scale, they were unadjusted. The threshold energies of **TS3-t-ax-2,6** and **TS3-c-ax-2,6** were fixed to their CASPT2 values.

Figure 3 shows the fit between the reinterpreted experimental and ME calculated **I1** decays, Table 4 gives the energies at the global χ^2 minimum, Figure 4 shows the sensitivity of the χ^2 minimum with respect to the stationary point energies, and Table 5 gives the phenomenological rate coefficients obtained from Bartis−Widom eigenvalue−eigenvector analysis of the ME results. As can be seen from the plots, the **I1** + O_2 energy minima are well-defined at 44 kJ mol^{-1}, which is in reasonable agreement with the previously discussed UCCSD(T)-ROHF/aug-cc-pVDZ value of 41 kJ mol^{-1}. Additionally, an energy of 44 kJ mol^{-1} for **I1** + O_2 gives a ΔH_0(298 K) for **I1** + O_2 $\leftrightarrows$ **I2-t-eq** of −52.56 kJ mol^{-1}, which is in good agreement with

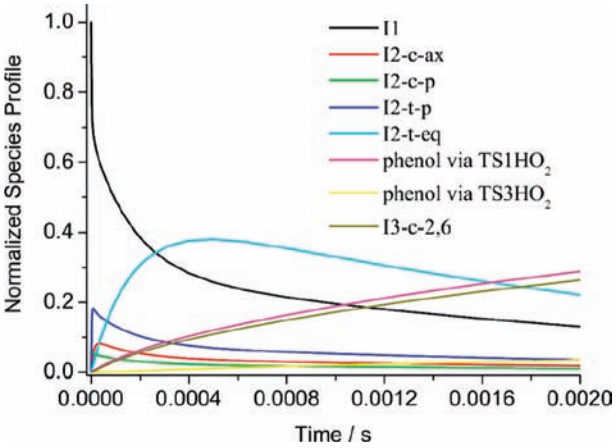

Figure 5. Time-dependent species profiles at the global minimum: 150 torr O_2, 298 K.

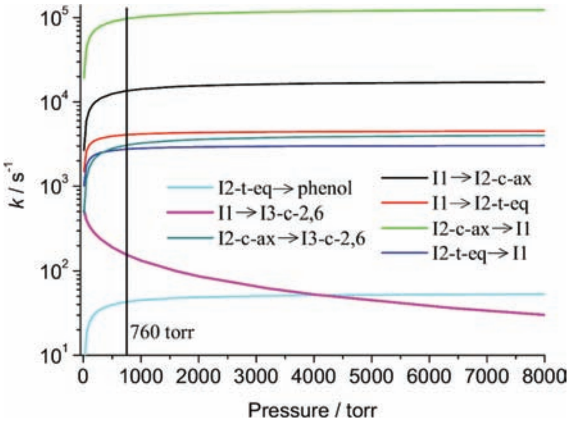

Figure 6. Phenomenological rates as a function of pressure for several reactions modeled in the ME: **I2-t-eq** → phenol + HO_2; **I1** → **I3-c-2,6**; **I2-c-ax** → **I3-c-2,6**; **I1** → **I2-c-ax**; **I1** → **I2-t-eq**; **I2-c-ax** → **I1**; and **I2-t-eq** → **I1**. All rate coefficients are first order except those which involve **I1**, in which case they are pseudo first order with $[O_2] = 5 \times 10^{18}$ molecule cm^{-3}.

the third law determined ΔH_0(298 K) value of -52.3 kJ mol^{-1} by Raoult et al. This observation appears to confirm that the long time equilibrium involves **I2-t-eq**. The χ^2 minimum for **TS3-HO$_2$** is at the limit of the search range; although, as Figure 4 shows, χ^2 is not very sensitive to this value.

Figure 5 shows the time-dependent profiles of significant species included in our ME calculations at the χ^2 minimum. The two main products are phenol and **I3-c-2,6**. The ME calculations with unadjusted stationary point energies give a phenol yield of 0.66 with 0.05 of the phenol yield obtained via **TS3-HO$_2$**, and the other 0.61 via **TS1-HO$_2$**. At the χ^2 minimum, the phenol yield is 0.55, with 0.06 of the yield obtained via **TS3-HO$_2$**. Under low $[NO_x]$ conditions, the 298 K phenol yields reported in the literature vary substantially. Atkinson et al. reported a yield of 0.236 ± 0.044, with no dependence on $[NO_x]$,[18] Bjergbakke et al.[62] reported yields of 0.25 ± 0.05, and Berndt et al.[63] reported yields of 0.23 ± 0.07 under NO_x-free conditions. In 2002, Volkamer et al.[5] used both FTIR spectrometry and differential optical absorption spectroscopy (DOAS) in two different environmental chambers and reported the phenol yield to be 0.53 ± 0.05 under low $[NO_x]$ conditions. Recently, Berndt and Böge performed measurements using FTIR spectrometry in a flow tube and reported yields of 0.61 ± 0.07.[30] Volkamer et al. discuss potential experimental artifacts accounting for the discrepancy of the higher phenol yield measurements with the earlier measurements. Following on from the study of Volkamer et al., Klotz et al.[20] investigated the phenol yield as a function of $[NO_x]$ and reported a phenol yield under zero $[NO_x]$ conditions of 0.55 ± 0.05, which decreases to <0.05 when $[NO_x]$ is as large as 2.25×10^{14} molecule cm^{-3}. The calculated phenol yield in this work is in agreement with the most recent experimental studies of Volkamer et al.,[5] Klotz et al.,[20] and Berndt and Böge.[30] Our calculations thus provide a theoretical basis for the experimentally observed high phenol yields.

Finally, we note that the phenomenological rate coefficients abstracted from our ME calculations indicate that the system is not at the high-pressure limit at 760 torr. Figure 6 shows several of the important phenomenological rate coefficients in this system as a function of pressure using stationary point energies at the χ^2 minimum. All of the reactions shown are still in the falloff at 760 torr. The pressure effect on the rate of **I1** → **I3-c-2,6**, which occurs without any intermediate stabilization in **I2-c-ax**, is particularly interesting. At the high-pressure limit, this rate coefficient goes to zero, the **I2-c-ax** → **I3-c-2,6** rate coefficient increases, and all of the **I3-c-2,6** is formed by isomerization from thermalized **I2-c-ax**. At atmospheric pressure, a small fraction of the **I3-c-2,6** is formed by this direct channel. In this system, the differences between most of the TST high-pressure limiting rate coefficients and the rate coefficients determined from a 760 torr ME are not greater than 10−20%. While this is not a dramatic effect, Figure 6 suggests that canonical TST (even at atmospheric pressure) will result in a small systematic overestimation of the rate coefficients. The significance of both direct and indirect kinetics is recognized in combustions systems,[64] but previous theoretical work on atmospheric aromatic oxidation has been oriented toward the calculation of free energy surfaces and TST rate coefficients, both of which imply that the system is at its high-pressure limit, and Maxwell−Boltzmann statistics are applicable to all regions of the PES.

III. Fate of the Bicyclic Radical. The later stages of benzene oxidation, which give glyoxal, are of considerable interest and are not well understood. The discussion above suggests that the fraction of benzene-OH that is not converted to phenol + HO_2 forms a bicyclic radical, **I3-c-2,6**. Following from this conclusion, we investigated subsequent channels regarding the fate of **I3-c-2,6**. Ghigo and Tonachini have presented the most thorough investigation of PES channels leading to the formation of unsaturated dialdehydes in benzene oxidation.[33] One of the channels to glyoxal formation proposed by these workers begins through reaction of the peroxy radical, **I2-c-ax** or **I2-t-eq**, with NO. [33] As discussed in the introduction and reaffirmed by the rate coefficients given in Table 5, **I2-c-ax** has a lifetime that is too short to react with NO under typical atmospheric concentrations. Competition between unimolecular reactions of **I2-t-eq** and its reaction with NO is only possible with [NO] higher than that which generally occurs in the atmosphere, making this channel unlikely to be important under typical atmospheric conditions. Therefore, likely routes to glyoxal formation concern the fate of **I3-c-2,6**.

In agreement with the work of Ghigo and Tonachini, we identified two possible reactions of **I3-c-2,6** using the G3X(MP2)-RAD model chemistry. The results are given in Table 6, and shown in Figure 7: **I3-c-2,6** may react with O_2 via **TS4-c(+O$_2$)** to give **I4-c(peroxy)**, or it may isomerize to give an epoxide, **I4-c(epoxide)**. The G3X(MP2)-RAD calculations for both **TS4-c(+O$_2$)** and **TS4-c** are considerably spin contaminated. The origin of the spin contamination in **TS4-c(+O$_2$)** is similar to that previously discussed for **TS1-c** and **TS1-t**, deriving from

TABLE 6: G3X(MP2)-RAD 0K Energies for the Reaction Paths Available to I3-c-2,6: Isomerization to I4-c(peroxy) and Addition of O_2[a]

path	stationary point	G3X(MP2)-RAD	T1	D1	$\langle S^2 \rangle$
O_2 addition	O_2 + I3-c-2,6	0.00	0.0255	0.1555	0.751
	TS4-c(+O_2)	10.07	0.0409	0.2834	0.984
	I4-c(peroxy)	−68.55	0.0226	0.1415	0.751
isomerization	I3-c-2,6	0.00	0.0255	0.1555	0.751
	TS4-c	73.87	0.0369	0.2331	0.756
	I4-c(peroxide)	−59.05	0.0171	0.0851	0.751

[a] For each path, the energy is in kJ mol^{-1}, and referenced to the reactants - either **I3-c-2,6** or O_2 + **I3-c-2,6**. The T1, D1, and $\langle S^2 \rangle$ values are obtained as described previously in Table 1.

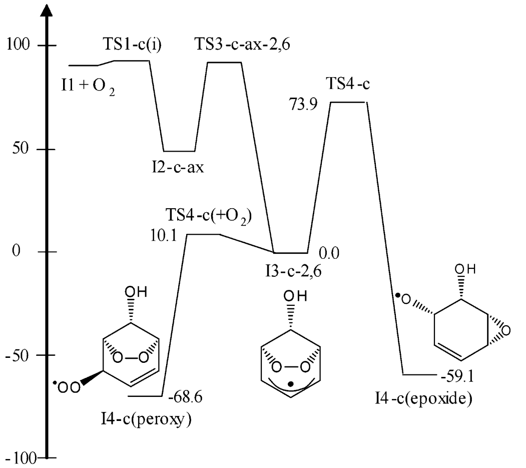

Figure 7. G3X(MP2)-RAD 0K PES diagram for the reaction paths available to **I3-c-2,6**: isomerization to **I4-c(peroxy)**, and addition of O_2.

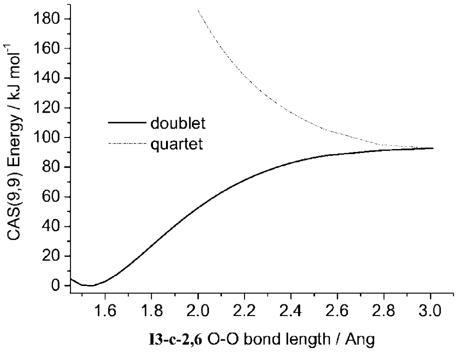

Figure 8. Results of a CASSF(9,9)/cc-pVDZ relaxed PES scan across the O−O bond in **I3-c-2,6** showing the energy of the doublet and quartet state at each scan geometry.

mixing with the $^1\Delta$ state of O_2, and the calculated G3X(MP2)-RAD energy for **TS4-c(+O_2)** is likely an overestimate. For TS4-c, there is a low-lying quartet state, and our calculations show a diradical plateau region of the PES similar to those recently reviewed by Carpenter.[65] Figure 8 shows the results of a relaxed PES scan along the O−O bond in **I3-c-2,6** at the CASSCF(9,9)/cc-pVDZ model chemistry for both the lowest doublet and quartet states. Using the CASSCF model chemisty, we located a conical intersection at an O−O bond length of 3.01 Å with an energy 92 kJ mol^{-1} above the bottom of the doublet **I3-c-2,6** well. At the CASPT2 model chemistry, the conical intersection is ~104 kJ mol^{-1} above the bottom of the doublet **I3-c-2,6** well. Passage through the conical intersection is likely insignificant in the atmosphere, given that it is ~18−30 kJ mol^{-1} higher in energy than **TS4-c**; nevertheless, it is low lying enough to affect the accuracy of the energy calculated for **TS4-c**.

To assess the relative importance of O_2 addition to **I3-c-2,6** versus isomerization to **I4-c(epoxide)**, we ran ME simulations identical to those described above but included two additional wells: **I3-c-2,6** and **I4-c(epoxide)**. Using the energies in Table 6, the TST rate coefficient for **I3-c-2,6** + O_2 via the G3X(MP2) barrier for **TS4-c(+O_2)** is 8.31×10^{-16} cm^3 molecule^{-1} s^{-1}. With atmospheric $[O_2] = 4.92 \times 10^{18}$, the pseudo-first-order rate constant for the addition of O_2 to **I3-c-2,6** is ~4090 s^{-1}, whereas the TST rate coefficient for **I3-c-2,6 → I4-c(epoxide)** via **TS4c** is ~1.0 s^{-1}. Therefore, a significant yield of the epoxide is only possible if there is a prompt formation channel; i.e., if it is formed directly from **I2-c-ax** without any intermediate stabilization in **I3-c-2,6**. Our ME calculations show the yield of epoxide to be ~1% via the prompt channel under atmospheric conditions. If the **TS4-c** barrier is lowered by 5 kJ mol^{-1}, then the **I3-c-2,6 → I4-c(epoxide)** channel remains unimportant, but the prompt epoxide yield increases to ~0.04. We were unable to locate a TS using the multireference methodology described for the structures in Table 3 and Figure 1; however, single-point CASPT2//CASSCF(9,9)/cc-pVDZ energy calculations on the G3X(MP2)-RAD geometries for both **I3-c-2,6** and **TS4-c** showed that the calculated **TS4-c** barrier height agreed with the G3X(MP2)-RAD barrier height within 2 kJ mol^{-1}. On the basis of these calculations, we cannot entirely rule out the formation of epoxides in benzene oxidation at atmospheric pressures, but the yields are likely small (i.e., less than 0.04 of the total product yield), and will be pressure dependent. At zero pressure, prompt formation of the epoxide will dominate any intermediate stabilization of **I3-c-2,6**.

Conclusions

In this article, we have calculated a very detailed PES for the initial stages of atmospheric benzene oxidation, reinterpreted the experimental **I1** decays, modeled them with the ME, and performed a sensitivity analysis within the uncertainty limits of the electronic structure theory calculations. This work offers a quantitative rationalization for the formation of bicyclic peroxy radicals. This study shows the complexity of the benzene oxidation PES at a level of detail not available in previous studies: besides the number of isomers and reaction paths available, the accuracy of single reference spin unrestricted electronic structure theory methods suffers spin contamination from state mixing, and higher level methods are necessary.

In addition to the direct abstraction channel to give phenol + HO_2, there are four addition paths for O_2 to **I1** so that the ME calculations show a multiexponential **I1** decay trace. For each isomer, only certain reaction paths are permitted: **I2-c-ax** readily undergoes cyclization to give a bridged bicyclic species, whereas **I2-t-eq** may undergo a concerted elimination via **I2-t-ax** to yield HO_2 + phenol. The results are consistent with the high phenol yields reported in recent experimental investigations[5,20,30] and offer a potential route to glyoxal formation through the bicyclic species. They also suggest that some of the HO_2 + phenol may be formed via a concerted elimination channel of HO_2 from **I2-t-eq**, which is a mechanistic feature that is compatible with experimental evidence showing decreasing phenol yields with increasing $[NO_x]$.[20] Assuming that **I2-t-eq** + NO has a 298 K rate constant of $(1.1 \pm 0.4) \times 10^{-11}$ cm^3 molecule^{-1} s^{-1},[22] then the **I2-t-eq** + NO pseudo-first-order rate constant is ~270 s^{-1} with 1 ppm NO, which is competitive with the rate of **I2-t-eq** → phenol + HO_2 given in Table 5. Recent experimental evidence also indicates that **I1** may react with NO_2

under high [NO_2] conditions, potentially affecting phenol yields.[15] Further modeling studies with chamber data sets at varying [NO] and [NO_2] may help to elucidate the relative significance of phenol formation routes via both the direct abstraction and concerted elimination channels.

Similar to the conclusions of Molina and coworkers in their theoretical examination of toluene oxidation,[41] our calculations suggest that the yield of epoxides under atmospheric conditions is small, although our calculated barriers show this channel to be more kinetically facile than their calculations. Therefore, it is likely that routes to glyoxal formation primarily concern the fate of **I3-c-2,6**. The glyoxal yields for benzene oxidation have been measured by Volkamer et al.[29] to be 0.352 ± 0.096, which broadly agrees with the **I3-c-2,6** yield calculated in this work of 0.45. The mechanism proposed in this work may serve to focus future theoretical investigations of both benzene and toluene oxidation. In both cases, routes to glyoxal formation appear to concern the fate of the bicyclic peroxy radicals, and further theoretical studies are needed. Further experimental work is also required: photolytic generation of **I1** and its subsequent measurement with fast time resolution may reveal the multi-exponential decay indicated by our ME calculations. Time-resolved measurements of other products, such as HO_2 and phenol, would also offer further constraints for rationalizing the mechanism.

Finally, we have shown that canonical TST may not be appropriate for obtaining a quantitative understanding of the dynamics that occur on the benzene oxidation PES because the reactive time scales are competitive with collisional deactivation time scales.

Acknowledgment. D.R.G. is grateful for an Overseas Research Studentship (Universities U.K.), a University of Leeds Tetley and Lupton scholarship, and funding from the EU EUROCHAMP program (RII3-CT-2004-505968). A substantial portion of the computational work was made possible by a grant from the National Service for Computational Chemistry Software (NSCCS). Thanks to Sarah Wilsey, Mike Robb, Martial Boggio-Pasqua, and Helen Tsui for support at NSCCS. Thanks to Alan Real for additional computing support as well as Jeremy Harvey, Steve Klippenstein, Larry Harding, and Andrew Rickard for helpful comments.

Supporting Information Available: Atom numbering scheme, CI coefficients greater than |0.05|, Lennard-Jones parameters, rotational constants and vibrational frequencies used in ME modelling, mathematical development of the methodology used for carrying out the sensitivity analysis, and optimized G3X Cartesian geometries for all of the structures discussed in the text. This material is available free of charge via the Internet at http://pubs.acs.org.

References and Notes

(1) Houweling, S.; Dentener, F.; Lelieveld, J. *J. Geophys. Res., [Atmos.]* **1998**, *103*, 10673.

(2) Calvert, J. G.; Atkinson, R.; Becker, K. H.; Kamens, R. M.; Seinfeld, J. H.; Wallington, T. J.; Yarwood, G. *The Mechanisms of Atmospheric Oxidation of Aromatic Hydrocarbons*; Oxford University Press: New York, 2002.

(3) Derwent, R. G.; Jenkin, M. E.; Saunders, S. M.; Pilling, M. J. *Atmos. Environ.* **1998**, *32*, 2429.

(4) Bloss, C.; Wagner, V.; Bonzanini, A.; Jenkin, M. E.; Wirtz, K.; Martin-Reviejo, M.; Pilling, M. J. *Atmos. Chem. Phys.* **2005**, *5*, 623.

(5) Volkamer, R.; Klotz, B.; Barnes, I.; Imamura, T.; Wirtz, K.; Washida, N.; Becker, K. H.; Platt, U. *Phys. Chem. Chem. Phys.* **2002**, *4*, 1598.

(6) Ghigo, G.; Tonachini, G. *J. Am. Chem. Soc.* **1999**, *121*, 8366.

(7) Forstner, H. J. L.; Flagan, R. C.; Seinfeld, J. H. *Environ. Sci. Technol.* **1997**, *31*, 1345.

(8) Finlayson-Pitts, B. J.; Pitts, J. N., Jr. *Science (Washington DC, U.S.)* **1997**, *276*, 1045.

(9) Bloss, C.; Wagner, V.; Jenkin, M. E.; Volkamer, R.; Bloss, W. J.; Lee, J. D.; Heard, D. E.; Wirtz, K.; Martin-Reviejo, M.; Rea, G.; Wenger, J. C.; Pilling, M. J. *Atmos. Chem. Phys.* **2005**, *5*, 641.

(10) Saunders, S.; Jenkin, M.; Derwent, R.; Pilling, M. *Atmos. Chem. Phys.* **2003**, *3*, 161.

(11) Jenkin, M. E.; Saunders, S. M.; Wagner, V.; Pilling, M. J. *Atmos. Chem. Phys.* **2003**, *3*, 181.

(12) Dodge, M. C. *Atmos. Environ.* **2000**, *34*, 2103.

(13) Johnson, D.; Jenkin, M. E.; Wirtz, K.; Martin-Reviejo, M. *Environ. Chem.* **2005**, *2*, 35.

(14) Martin-Reviejo, M.; Wirtz, K. *Environ. Sci. Technol.* **2005**, *39*, 1045.

(15) Koch, R.; Knispel, R.; Elend, M.; Siese, M.; Zetzsch, C. *Atmos. Chem. Physics.* **2007**, *7*, 2057.

(16) Zhao, J.; Zhang, R.; Misawa, K.; Shibuya, K. *J. Photochem. Photobiol., A* **2005**, *176*, 199.

(17) Smith, D. F.; Kleindienst, T. E.; McIver, C. D. *J. Atmos. Chem.* **1999**, *34*, 339.

(18) Atkinson, R.; Aschmann, S. M. *Int. J. Chem. Kinet.* **1994**, *26*, 929.

(19) Kwok, E. S. C.; Aschmann, S. M.; Atkinson, R.; Arey, J. *J. Chem. Soc., Faraday Trans.* **1997**, *93*, 2847.

(20) Klotz, B.; Volkamer, R.; Hurley, M. D.; Andersen, M. P. S.; Nielsen, O. J.; Barnes, I.; Imamura, T.; Wirtz, K.; Becker, K.-H.; Platt, U.; Wallington, T. J.; Washida, N. *Phys. Chem. Chem. Phys.* **2002**, *4*, 4399.

(21) Lin, S.-C.; Kuo, T.-C.; Lee, Y.-P. *J. Chem. Phys.* **1994**, *101*, 2098.

(22) Bohn, B.; Zetzsch, C. *Phys. Chem. Chem. Phys.* **1999**, *1*, 5097.

(23) Uc, V. H.; Alvarez-Idaboy, J. R.; Galano, A.; Vivier-Bunge, A. *J. Phys. Chem. A* **2008**, *112*, 7608.

(24) Chen, C.-C.; Bozzelli, J. W.; Farrell, J. T. *J. Phys. Chem. A* **2004**, *108*, 4632.

(25) Raoult, S.; Rayez, M.-T.; Rayez, J.-C.; Lesclaux, R. *Phys. Chem. Chem. Phys.* **2004**, *6*, 2245.

(26) Johnson, D.; Raoult, S.; Rayez, M.-T.; Rayez, J.-C.; Lesclaux, R. *Phys. Chem. Chem. Phys.* **2002**, *4*, 4678.

(27) Grebenkin, S. Y.; Krasnoperov, L. N. *J. Phys. Chem. A* **2004**, *108*, 1953.

(28) Gomez Alvarez, E.; Viidanoja, J.; Munoz, A.; Wirtz, K.; Hjorth, J. *Environ. Sci. Technol.* **2007**, *41*, 8362.

(29) Volkamer, R.; Platt, U.; Wirtz, K. *J. Phys. Chem. A* **2001**, *105*, 7865.

(30) Berndt, T.; Boege, O. *Phys. Chem. Chem. Phys.* **2006**, *8*, 1205.

(31) Lay, T. H.; Bozzelli, J. W.; Seinfeld, J. H. *J. Phys. Chem.* **1996**, *100*, 6543.

(32) Ghigo, G.; Tonachini, G. *J. Am. Chem. Soc.* **1998**, *120*, 6753.

(33) Motta, F.; Ghigo, G.; Tonachini, G. *J. Phys. Chem. A* **2002**, *106*, 4411.

(34) Sousa, S. F.; Fernandes, P. A.; Ramos, M. J. *J. Phys. Chem. A* **2007**, *111*, 10439.

(35) Curtiss, L. A.; Redfern, P. C.; Raghavachari, K.; Pople, J. A. *J. Chem. Phys.* **2001**, *114*, 108.

(36) Henry, D. J.; Sullivan, M. B.; Radom, L. *J. Chem. Phys.* **2003**, *118*, 4849.

(37) Werner, H.-J. *Mol. Phys.* **1996**, *89*, 645.

(38) Celani, P.; Werner, H.-J. *J. Chem. Phys.* **2000**, *112*, 5546.

(39) Frankcombe, T. J.; Smith, S. C. *J. Phys. Chem. A* **2007**, *111*, 3686.

(40) Frankcombe, T. J.; Smith, S. C. *J. Phys. Chem. A* **2007**, *111*, 3691.

(41) Suh, I.; Zhang, R.; Molina, L. T.; Molina, M. J. *J. Am. Chem. Soc.* **2003**, *125*, 12655.

(42) Suh, I.; Zhao, J.; Zhang, R. *Chem. Phys. Lett.* **2006**, *432*, 313.

(43) Curtiss, L. A.; Carpenter, J. E.; Raghavachari, K.; Pople, J. A. *J. Chem. Phys.* **1992**, *96*, 9030.

(44) Miller, J. A. *Faraday Discuss.* **2001**, *119*, 461.

(45) Frisch, M. J.; Trucks, G. W.; Schlegel, H. B.; Scuseria, G. E.; Robb, M. A.; Cheeseman, J. R.; Montgomery, J. A., Jr.; Vreven, T.; Kudin, K. N.; Burant, J. C.; Millam, J. M.; Iyengar, S. S.; Tomasi, J.; Barone, V.; Mennucci, B.; Cossi, M.; Scalmani, G.; Rega, N.; Petersson, G. A.; Nakatsuji, H.; Hada, M.; Ehara, M.; Toyota, K.; Fukuda, R.; Hasegawa, J.; Ishida, M.; Nakajima, T.; Honda, Y.; Kitao, O.; Nakai, H.; Klene, M.; Li, X.; Knox, J. E.; Hratchian, H. P.; Cross, J. B.; Bakken, V.; Adamo, C.; Jaramillo, J.; Gomperts, R.; Stratmann, R. E.; Yazyev, O.; Austin, A. J.; Cammi, R.; Pomelli, C.; Ochterski, J. W.; Ayala, P. Y.; Morokuma, K.; Voth, G. A.; Salvador, P.; Dannenberg, J. J.; Zakrzewski, V. G.; Dapprich, S.; Daniels, A. D.; Strain, M. C.; Farkas, O.; Malick, D. K.; Rabuck, A. D.; Raghavachari, K.; Foresman, J. B.; Ortiz, J. V.; Cui, Q.; Baboul, A. G.; Clifford, S.; Cioslowski, J.; Stefanov, B. B.; Liu, G.; Liashenko, A.; Piskorz, P.; Komaromi, I.; Martin, R. L.; Fox, D. J.; Keith, T.; Al-Laham, M. A.; Peng, C. Y.; Nanayakkara, A.; Challacombe, M.; Gill, P. M. W.; Johnson, B.; Chen, W.; Wong, M. W.; Gonzalez, C.; Pople, J. A. *Gaussian 03*, revision B.03; Gaussian, Inc.: Wallingford, CT, 2004.

(46) DeYonker, N. J.; Cundari, T. R.; Wilson, A. K. *J. Chem. Phys.* **2006**, *124*, 114104/1.

(47) Dennington, R., II.; Keith, T.; Millam, J.; Eppinnett, K.; Hovell, W. L.; Gilliland, R. *GaussView*, version 3.09; Semichem, Inc: Shawnee Mission, KS, 2003.

(48) Jensen, F. *Introduction to Computational Chemistry*, 2nd ed.; John Wiley & Sons: Chichester, U.K., 2007.

(49) Werner, H.-J.; Knowles, P. J.; Lindh, R.; Manby, F. R.; Schütz; M.; Celani, P.; Korona, T.; Rauhut, G.; Amos, R. D.; Bernhardsson, A.; Berning, A.; Cooper, D. L.; Deegan, M. J. O.; Dobbyn, A. J.; Eckert, F.; Hampel, C.; Hetzer, G.; Lloyd, A. W.; McNicholas, S. J.; Meyer, W.; Mura, M. E.; Nicklauss, A.; Palmieri, P.; Pitzer, R.; Schumann, U.; Stoll, H.; Stone, A. J.; Tarroni, R. MOLPRO, version 2006 1;a package of ab initio programs, see www.molpro.net.

(50) Dunning, T. H., Jr. *J. Chem. Phys.* **1989**, *90*, 1007.

(51) Schaftenaar, G.; Noordik, J. H. *J. Comput.-Aided Molec. Des.* **2000**, *14*, 123.

(52) McKee, K. W.; Blitz, M. A.; Cleary, P. A.; Glowacki, D. R.; Pilling, M. J.; Seakins, P. W.; Wang, L. *J. Phys. Chem. A* **2007**, *111*, 4043.

(53) Miller, J. A.; Klippenstein, S. J. *J. Phys. Chem. A* **2006**, *110*, 10528.

(54) Holbrook, K. A.; Pilling, M. J.; Robertson, S. H. *Unimolecular Reactions*; 2nd ed.; Wiley: Chichester, U.K., 1996.

(55) Bartis, J. T.; Widom, B. *J. Chem. Phys.* **1974**, *60*, 3474.

(56) Robertson, S. H.; Pilling, M. J.; Jitariu, L. C.; Hillier, I. H. *Phys. Chem. Chem. Phys.* **2007**, *9*, 4085.

(57) Robertson, S. H.; Glowacki, D. R.; Liang, C.-H.; Morley, C. M., Pilling, M. J. *MESMER (Master Equation Solver for Multi-Energy Well Reactions)*, 2008; an object oriented C++ program for carrying out ME calculations and eigenvalue−eigenvector analysis on arbitrary multiple well systems. http://sourceforge.net/projects/mesmer.

(58) Lee, T. J. *Chem. Phys. Lett.* **2003**, *372*, 362.

(59) Walch, S. P. *Chem. Phys. Lett.* **1993**, *215*, 81.

(60) Gannon, K. L.; Glowacki, D. R.; Blitz, M. A.; Hughes, K. J.; Pilling, M. J.; Seakins, P. W. *J. Phys. Chem. A* **2007**, *111*, 6679.

(61) Baeza-Romero, M. T.; Glowacki, D. R.; Blitz, M. A.; Heard, D. E.; Pilling, M. J.; Rickard, A. R.; Seakins, P. W. *Phys. Chem. Chem. Phys.* **2007**, *9*, 4114.

(62) Bjergbakke, E.; Sillesen, A.; Pagsberg, P. *J. Phys. Chem.* **1996**, *100*, 5729.

(63) Berndt, T.; Boge, O.; Herrmann, H. *Chem. Phys. Lett.* **1999**, *314*, 435.

(64) Knepp, A. M.; Meloni, G.; Jusinski, L. E.; Taatjes, C. A.; Cavallotti, C.; Klippenstein, S. J. *Phys. Chem. Chem. Phys.* **2007**, *9*, 4315.

(65) Carpenter, B. K. *Annu. Rev. Phys. Chem.* **2005**, *56*, 57.

JP9001466